Early Dynamic ^{18}F-FDG PET to Detect Hyperperfusion in Hepatocellular Carcinoma Liver Lesions

Jan-Henning Schierz[1], Thomas Opfermann[1], Jörg Steenbeck[1], Eric Lopatta[2], Utz Settmacher[3], Andreas Stallmach[4], Robert J. Marlowe[5], and Martin Freesmeyer[1]

[1]Clinic of Nuclear Medicine, Jena University Hospital, Jena, Germany; [2]Institute of Diagnostic and Interventional Radiology, Jena University Hospital, Jena, Germany; [3]Clinic of General, Visceral and Vascular Surgery, Jena University Hospital, Jena, Germany; [4]Clinic of Internal Medicine II, Department of Gastroenterology, Hepatology and Infectious Diseases, Jena University Hospital, Jena, Germany; and [5]Spencer-Fontayne Corporation, Jersey City, New Jersey

In addition to angiographic data on vascularity and vascular access, demonstration of hepatocellular carcinoma (HCC) liver nodule hypervascularization is a prerequisite for certain intrahepatic antitumor therapies. Early dynamic (ED) ^{18}F-FDG PET/CT could serve this purpose when the current standard method, contrast-enhanced (CE) CT, or other CE morphologic imaging modalities are unsuitable. A recent study showed ED ^{18}F-FDG PET/CT efficacy in this setting but applied a larger-than-standard ^{18}F-FDG activity and an elaborate protocol likely to hinder routine use. We developed a simplified protocol using standard activities and easily generated visual and descriptive or quantitative endpoints. This pilot study assessed the ability of these endpoints to detect HCC hyperperfusion and, thereby, evaluated the suitability in of the protocol everyday practice. **Methods:** Twenty-seven patients with 34 HCCs (diameter $\geq$ 1.5 cm) with hypervascularization on 3-phase CE CT underwent liver ED ^{18}F-FDG PET for 240 s, starting with ^{18}F-FDG (250-MBq bolus injection). Four frames at 15-s intervals, followed by 3 frames at 60-s intervals were reconstructed. Endpoints included focal tracer accumulation in the first 4 frames (60 s), subsequent focal washout, and visual and quantitative differences between tumor and liver regions of interest in maximum and mean ED standardized uptake value (ED SUVmax and ED SUVmean, respectively) 240-s time–activity curves. **Results:** All 34 lesions were identified by early focal ^{18}F-FDG accumulation and faster time-to-peak ED SUVmax or ED SUVmean than in nontumor tissue. Tumor peak ED SUVmax and ED SUVmean exceeded liver levels in 85% and 53%, respectively, of lesions. Nadir tumor signal showed no consistent pattern relative to nontumor signal. HCC had a significantly shorter time to peak and significantly faster rate to peak for both ED SUVmax and ED SUVmean curves and a significantly higher peak ED SUVmax but not peak ED SUVmean than the liver. **Conclusion:** This pilot study provided proof of principle that our simplified ED ^{18}F-FDG PET/CT protocol includes endpoints that effectively detect HCC hypervascularization; this finding suggests that the protocol can be used routinely.

The liver has dual vascularization, with approximately 75%–80% of blood supplied by the portal vein and the remaining 20%–25% by the hepatic artery. However, many liver neoplasia, especially hepatocellular carcinomas (HCCs), are characterized by nearly exclusively arterial perfusion (*1*). Consequently, these tumors are usually arterially hypervascularized, compared with noncancerous liver tissue (*2*).

In addition to angiographic data on vascularity and vascular access, demonstration of arterial hypervascularization in HCC liver lesions is a prerequisite for intrahepatic anti-HCC interventions such as transarterial chemoembolization or selective internal radiotherapy. In these interventions, catheter-based embolic agents are introduced into the hyperperfused tumor regions via the femoral artery and, ultimately, the hepatic artery branches (*3*).

Contrast-enhanced (CE) morphologic imaging modalities, most commonly CT but also ultrasonography or MR imaging, currently are the preferred methods to initially demonstrate HCC arterial hypervascularization. The underlying principle is the imaging, quantitation, or both of the early influx of the contrast medium to show the increased arterial blood supply and of the washout to show the missing portal vascularization (*4–6*).

However, these modalities sometimes may be unsuitable. CT contrast medium is frequently poorly tolerated, especially in patients with hyperthyroid or renal comorbidity (*7–10*), and the relatively high radiation dose of even state-of-the-art 3-phase CE CT may be problematic for the liver, especially in younger patients (*11*). Ultrasonographic contrast medium carries a risk of allergic reactions and is contraindicated in patients with pronounced cardiac problems such as unstable angina pectoris or heart failure (*12*), and

ultrasonography may poorly image deep-lying lesions, especially in the obese. MR imaging contrast medium cannot be given to those with renal failure, and MR imaging cannot be performed in patients with implanted electronic devices, certain ferromagnetic metal implants, or intractable claustrophobia (13).

Because only approximately 50%–70% of HCC tumors exhibit glucose metabolism higher than that of the liver parenchyma (14,15), conventional late static whole-body (WB) ^{18}F-FDG PET combined with CT plays a subordinate role in HCC primary diagnosis. However, this procedure is often used to help confirm liver transplant eligibility by excluding extrahepatic tumor (16,17).

Performing early dynamic (ED) liver ^{18}F-FDG PET/CT before the conventional static WB procedure could provide an alternative for detecting HCC hypervascularization in patients with contraindications to CE morphologic imaging. After Mullani et al. (18) demonstrated the efficacy of ED ^{18}F-FDG PET/CT to measure blood flow in a variety of advanced solid tumors, Bernstine et al. (19) successfully applied the modality to assess HCC liver lesion perfusion. However, the Bernstine group used an elaborate protocol requiring laborious, time-consuming calculation that likely precludes the use of the protocol in everyday practice. Additionally, they administered a relatively large ^{18}F-FDG activity, 500 MBq. Such a tracer amount substantially increases radiation exposure, compared with that associated with the approximately 250-MBq activity recommended by the guidelines of the European Association of Nuclear Medicine (20), and at our center a larger activity also increases per-procedure costs by approximately $325–390 (U.S. dollars; ~250–300 Euros) relative to use of the smaller activity.

We therefore formulated a simplified, lower-activity liver ED ^{18}F-FDG PET/CT protocol including a variety of easily generated potential visual and descriptive or quantitative endpoints. We performed the present pilot study to assess the ability of the endpoints to detect hypervascularized HCC liver lesions and thus the suitability of the protocol for everyday use.

MATERIALS AND METHODS

Study Comparison and Endpoints

The study compared HCC nodules versus adjoining or nearby tumor-free liver tissue, each represented by respective regions of interest (ROIs), regarding the ED ^{18}F-FDG PET endpoints summarized in Table 1. The endpoints were chosen for analogy with evaluation of 3-phase CE CT images for HCC hypervascularization. The comparison was performed by 2 experienced nuclear medicine specialists on a nonmasked, consensus basis.

As a preliminary step enabling the comparison, hypervascularized tumors were identified on liver ED ^{18}F-FDG PET images. With the aid of software (Volumetric Analysis; Siemens) for analyzing data acquired in list mode, the ED PET data were presented on a dedicated multimodal evaluation console (Syngo MMWP Version VE31A; Siemens), and the images for all time intervals were visually scanned for increased tracer accumulation. A focal accumulation within any of the earliest 4 frames (together representing the

first 60 s of scanning) was taken to denote hypervascularization. All layers of the focal finding then were evaluated to demarcate actual foci from tubular vessel sections. Next, the focal accumulation signal was visually evaluated for signs of tracer washout in all frames (together representing the first 240 s after tracer injection) in chronologic order. Washout was defined as a downward trend in signal intensity in the focal finding after peak signal intensity had been attained. All findings of hypervascularized tumors were confirmed morphologically, through side-by-side comparison with a CE CT scan, because the Volumetric Analysis software did not support presentation of an ^{18}F-FDG PET/CT hybrid image.

After morphologic confirmation of the ED PET finding of a hypervascularized tumor, a 2-dimensional ROI was drawn over the entire lesion. For each tumor, a 2-dimensional ROI of similar size was drawn over a nearby and, if possible, adjoining tumor-free liver region, using transaxial or coronal sections depending on the location of the tumor. To avoid confounding our comparisons, we made every effort to exclude from the nontumor ROIs larger hepatic vessels or regions showing textural abnormalities on CE CT, which might represent cirrhotic tissue with increased vascular resistance relative to normal hepatic parenchyma.

Time–activity curves for the maximum ED ^{18}F-FDG PET standardized uptake value (ED SUVmax) and the mean ED ^{18}F-FDG PET standardized uptake value (ED SUVmean) of the tumor ROI and the nontumor ROI then were calculated for the ED ^{18}F-FDG PET scanning period and presented. The standardized uptake value (SUV) was determined by dividing the measured tracer concentration by total injected activity and body weight. The SUVmax was derived from the single voxel with the highest tracer uptake within an ROI and thus avoided bias introduced by the ROI size—that is, inclusion of a greater or lesser proportion of voxels with more intense or less intense uptake. The SUVmean was derived from all voxels within the ROI and thus was presumed to more closely reflect tracer uptake in that ROI as seen by the human eye.

We also performed conventional late static WB ^{18}F-FDG PET and visually evaluated the images regarding tumor demarcation and a morphologic correlate for focal findings. Additionally, we compared conventional WB ^{18}F-FDG PET data for tumor versus tumor-free liver ROIs, selected as described above, using the quantitative endpoints of peak SUVmax and peak SUVmean.

Patients, Lesions, and Ethics

The study sample comprised 27 consecutive adults with HCC that had been confirmed clinically, histologically, or both, who had at least 1 hypervascular HCC liver nodule 1.5 cm or greater in diameter on the CE CT. These patients were referred to our center from November 2010 to October 2011 for WB ^{18}F-FDG PET/CT to exclude extrahepatic involvement, thereby confirming eligibility for liver transplantation. Twenty-one patients had 1 such nodule each, and 6 patients 2–3 such nodules each, accounting for 34 lesions in total; patients tended to have few lesions because they were possible liver transplantation candidates. These tumors measured 5.6 ± 4.0 (mean ± SD; range, 1.6–15.0) cm in diameter. No patient had an HCC nodule less than 1.5 cm on CE CT images. Table 2 shows other key cohort characteristics, which were typical of the population with HCC undergoing WB ^{18}F-FDG PET/CT at our tertiary referral center. Our ED ^{18}F-FDG PET protocol conformed to the ethical guidelines of the 1975 Declaration of Helsinki and was approved by our hospital's Ethics Committee; all patients provided written informed consent.

TABLE 1
Liver ED ^{18}F-FDG PET Endpoints

Type of assessment	Endpoint
Descriptive (visual) comparison of tracer influx during first 4 frames (first 60 s of scanning)	Presence of focal accumulation in hypervascularized tumor sites that had been shown by CE CT
Descriptive (visual) comparison of tracer efflux during last 3 frames (61–240 s after tracer administration)	Presence of downward trend in signal intensity in areas of focal accumulation indicative of washout
Descriptive (visual) comparison of tracer influx: tumor vs. nontumor ROI time–activity curves	On the basis of shape of the curves:
	Time-to-peak ED SUV*max
	Time-to-peak ED SUVmean
	Magnitude of peak ED SUVmax
	Magnitude of peak ED SUVmean
Quantitative comparison of tracer influx: tumor vs. nontumor ROI time–activity curves	Time-to-peak ED SUVmax (s)
	Time-to-peak ED SUVmean (s)
	Peak ED SUVmax peak ED SUVmean
	Peak ED SUVmean
	Rate-to-peak ED SUVmax (i.e., ED SUVmax/time-to-peak ED SUVmax, SUV/s)
	Rate-to-peak ED SUVmean (i.e., ED SUVmean/time-to-peak ED SUVmean, SUV/s)
Descriptive (visual) comparison of tracer washout: tumor vs. nontumor ROI time–activity curves	On the basis of shape of the curves:
	Magnitude of washout

*SUV was calculated by dividing measured tracer concentration by total injected activity and body weight.

ED ^{18}F-FDG PET/CT and WB ^{18}F-FDG PET/CT

^{18}F-FDG (250 MBq) was administered in 10 mL of 0.9% saline as a 4 mL/s bolus, followed by rinsing with the same amount and concentration of saline. Patients fasted 8 h or more before ^{18}F-FDG administration, which occurred only if blood glucose measured less than 10 mmol/L at 20 min before the scheduled injection. Ten minutes before tracer application, butylscopolamine (5 mg) was given to relax the colon. The patient was positioned in the PET/CT system (Biograph mCT 40 with a TrueV fourth PET ring and a 21.8-cm axial field-of-view; Siemens) so that the liver was as fully as possible within the scanning area. Subsequently, a non-CE, low-dose liver CT (50 mAs, 120-kV tube voltage) image was obtained for attenuation correction. Images were reconstructed with a 3-mm slice thickness and a 1.5-mm increment. The radiation exposure attributable to the CT was approximately 0.3 mSv.

ED ^{18}F-FDG PET imaging was performed in list mode—that is, as continuous scanning with every measured value stored as raw data with an exact time stamp, beginning simultaneously with the ^{18}F-FDG bolus and continuing for 240 s. Subsequently, we reconstructed the data as 4 frames at 15-s intervals, followed by 3 frames at 60-s intervals. The frames were reconstructed using HD-TrueX software (Siemens), by 3-dimensional attenuation-weighted ordered-subset expectation maximization (4 iterations, 12 subsets) with a 5-mm postreconstruction gaussian filter, attenuation image segmentation, and a 200 × 200 pixel matrix. The initial short intervals were intended to take into account the arterial phase of rapid tracer influx, whereas the later pictures reconstructed over a longer period were intended to present with better counting statistics the venous phase and late venous phase of relatively slower tracer efflux.

Five minutes after the ED ^{18}F-FDG PET imaging was complete (~10 min after tracer application), furosemide (20 mg) was injected to flush the kidneys and thereby minimize genitourinary tract imaging artifacts in the subsequent static WB ^{18}F-FDG PET. The patient then was transferred prone to a waiting room and remained there until returning to the scanner for the latter procedure, performed at approximately 60–90 min after tracer injection. To avoid the interruption of workflow, ED PET data for 1 patient were reconstructed and transferred to the processing workstation while the PET system was disinfected and bed linens were changed for the next patient.

The WB ^{18}F-FDG PET/CT scanning region encompassed the base of the skull to the proximal thigh. Immediately before WB ^{18}F-FDG PET, a second low-dose CT scan (estimated radiation

TABLE 2
Key Patient Characteristics ($n = 27$)

Variable	Value
Men (n)	21 (85%)
Age (y)	
Mean ± SD	63.0 ± 7.1
Range	42–79
Serum α-fetoprotein (µg/L)	
Mean ± SD	40,862 ± 138,265
Range	2–708,360
CE CT findings (n)	
Cirrhosis	27
Riedel's lobe	3
Hepatomegaly	2

exposure, ~1.5 mSv) was obtained for attenuation correction, with the same settings as were used for the initial low-dose CT scan. As soon as possible thereafter, the WB ^{18}F-FDG PET scan was acquired with 6 bed positions at 2 min of recording time each, using identical image reconstruction methodology as for the ED ^{18}F-FDG PET scan.

CE CT

The CE CT scan used as a morphologic reference for the ^{18}F-FDG PET study was obtained as part of routine evaluation approximately 2 wk before the ^{18}F-FDG PET scan. The first step was to obtain a topogram from the base of the skull to the proximal thigh to determine the CE CT scanning area. That area usually was from the neck to the lower liver margin for the arterial phase and from the upper liver margin to the lower margin of the pelvis for the venous phase. After a bolus injection of 100 mL of contrast agent (Ultravist 300; Bayer Vital), the multislice CE CT scanning was performed as a bolus tracking technique. Tube voltage was 120 kV, the modulated tube current–time product was 80–280 mAs, and the section thickness was 0.625 mm; the image was reconstructed every 5 mm.

Statistics

Because this was a pilot comparison, no sample size calculations were performed. The significance of differences between tumor and nontumor ROIs was assessed with the Sign and Wilcoxon tests. All means are presented along with the SD. A P value of less than 0.05 was considered to show significance. SPSS Statistics software (version 19; IBM) was used for the analyses.

RESULTS

Representative images and time–activity curves are presented in Figures 1–4 (CE CT images in Fig. 1; ED ^{18}F-FDG PET images in Fig. 2; ED ^{18}F-FDG PET/CT images in Fig. 3; and tumor and liver ROIs and their ED SUVmax and ED SUVmean time–activity curves in Fig. 4).

Visual Evaluation of ED PET Images

On the basis of focal tracer accumulation in the first 60 s of scanning, every hypervascular tumor 1.5 cm or greater in diameter (34/34, 100%) that had been identified on CE CT was detectable on ED ^{18}F-FDG PET; the quality of presentation of the focal signal increase was independent of tumor size. On the basis of visual observation, during washout, the focal signal fell to a liver-equivalent level in 31 lesions (91%) and to below liver level in 1 lesion; washout was not discernible throughout the 240-s scanning period in the remaining 2 lesions.
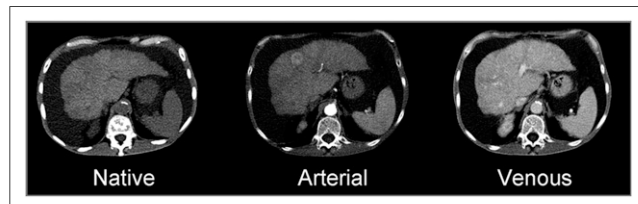

FIGURE 1. CE CT images of 2-cm-wide segment VIII tumor showing arterial hypervascularization and isointense presentation in venous phase.
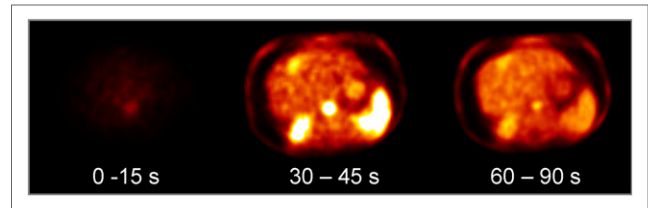

FIGURE 2. ED ^{18}F-FDG PET images of same tumor showing relatively slow tracer influx in aorta and good tumor visibility in arterial and venous time windows.

Descriptive Evaluation of Tumor Versus Nontumor Time–Activity Curves

As seen in Table 3, an earlier peak ED SUVmax and an earlier peak ED SUVmean for tumor foci than for nearby or adjoining tumor-free liver tissue could be seen on the basis of the shape of the corresponding time–activity curves for all 34 lesions. The magnitude of ED SUV elevation seemed to less reliably indicate a hypervascularized tumor: a higher peak was apparent on many but not all of the lesion ED SUVmax time–activity curves and on only just above half the lesion ED SUVmean curves, relative to their tumor-free comparator curves. The peaks of both the ED SUVmax and the ED SUVmean were higher in tumor than in parenchyma in 16 tumors (47%); all 34 tumors had either a peak ED SUVmax or a peak ED SUVmean higher than that of the corresponding nontumor ROI. No consistent visual washout pattern was evident for tumor tissue relative to nontumor liver tissue on the time–activity curves for either ED SUVmax or ED SUVmean.

Quantitative Evaluation of Tumor Versus Nontumor Time–Activity Curves

Table 4 summarizes quantitative variables related to ED SUV time–activity curves. On average, the time to peak ED SUVmax was 57 ± 37 s shorter in tumor than in nontumor tissue, a significant difference. Additionally, the peak ED SUVmax was significantly higher, and the ED SUVmax rose to peak level significantly more rapidly in tumor than in nontumor tissue. ED SUVmean also rose to peak level significantly more rapidly in tumor than in nontumor tissue. However, although the peak ED SUVmean was higher in tumor than in tumor-free liver tissue, that difference did not attain statistical significance.

Evaluation of WB ^{18}F-FDG PET/CT

For the WB ^{18}F-FDG PET/CT, the tumor, compared with parenchymal tissue, showed increased glucose metabolism in 20 of 34 cases (59%). On average, SUVmax was significantly higher in tumor than in nontumor tissue (4.7 ± 2.2 vs. 3.5 ± 0.7, $P < 0.05$, Sign test), as was the SUVmean (3.1 ± 0.9 vs. 2.6 ± 0.3, $P < 0.05$, Sign test).

DISCUSSION

Theoretically, adding a liver ED ^{18}F-FDG PET/CT before a late static WB ^{18}F-FDG PET/CT, which would be performed to exclude HCC extrahepatic spread, provides an
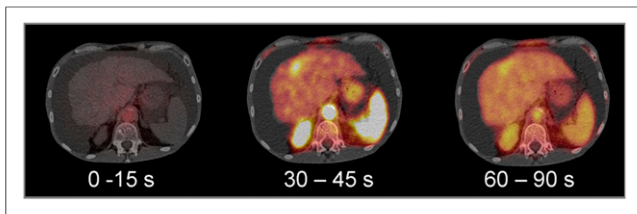
FIGURE 3. Secondary fusion of CT and ED ^{18}F-FDG PET images showing topographic correlation between both examinations.

appealing alternative for demonstrating HCC liver nodule hypervascularization when CE morphologic imaging is infeasible. Indeed, even when such imaging is feasible, ED ^{18}F-FDG PET has several advantages. The modality avoids the morbidity, discomfort, and prophylaxis to improve tolerability that are associated with contrast agents and, unlike MR imaging, is compatible with pacemakers and other implants. Additionally, ED ^{18}F-FDG PET has essentially no contraindications other than pregnancy, minimizing blood sampling, laboratory work, and anamnesis to determine eligibility.

The suitability of liver ED ^{18}F-FDG PET/CT for demonstrating HCC hypervascularization recently was elegantly demonstrated by Bernstine et al. (*19*), but the complexity of their protocol limits its routine applicability. Additionally, compared with standard activities, their unusually large ^{18}F-FDG activity increases patient radiation exposure by approximately 5 mSv, approximately the normal yearly radiation exposure and, at our center, increases cost by approximately $325–390 (U.S. dollars; ~250–300 Euros).

The present protocol therefore simplified that of Bernstine et al. (*19*) in 2 main ways. First, using ED ^{18}F-FDG PET/CT to generate CE CT–like images—that is, to depict the arterial, portal venous, and venous phases—and relying largely on simple visual and descriptive endpoints, we reconstructed fewer frames with longer times: 4 frames at 15-s intervals, then 3 frames at 60-s intervals, versus 18 frames at 5-s intervals. Our frame selection compromised the ability to limit computation time and effort, compared with obtaining sufficient temporal resolution, and the ability to generate adequate count statistics. In preliminary experiments, we found reconstruction of 5-s frames over 240 s to require at least 32 min and as long as 45 min, during which no further patients could be examined on the PET/CT system (unpublished data). In contrast, reconstruction with 15- and 60-s frames required only 7 min, allowing integration into our

routine workflow. We hypothesized that 15-s frames would be short enough to detect hypervascularized tumors yet long enough to smooth irregular curves caused by respiratory motion and to differentiate well between tumor and nontumor ED SUV curves.

Second, as endpoints, we substituted more easily determined visual and descriptive and qualitative variables for complex estimations of tumoral and nontumoral hepatic blood flow using an arterial input function.

Another noteworthy difference between our protocol and that of Bernstine et al. was that we worked with a lower, more standard (*20*) ^{18}F-FDG activity and a faster injection rate and injection: 250 MBq at 100 MBq/s, for a 2.5-s bolus versus 500 MBq at 50 MBq/s, for a 10-s bolus. We thereby sought to produce well-distinguishable curves despite the use of standard ^{18}F-FDG activities.

The present results provide proof of principle that our protocol indeed includes endpoints highly effective in detecting HCC liver lesion arterial hypervascularization: focal tracer influx during the first 4 frames (60 s of scanning) and ED SUVmax or ED SUVmean time–activity curves peaking earlier in a tumor ROI than in a liver ROI (Table 3) identified all 34 hypervascularized HCC nodules shown on CE CT, the current standard modality to demonstrate hyperperfusion in this setting. This discriminative ability confirms that our frame duration provided sufficient temporal resolution and, together with the 7-min frame reconstruction time and absence of apparent ED ^{18}F-FDG PET/CT-related toxicity in our patients, suggests that our protocol—perhaps with additional streamlining—may be suitable for routine use in settings in which list-mode evaluation software and PET systems capable of list-mode acquisition are available.

On visual image examination, the postpeak signal appeared to fall only to parenchymal levels in 33 of 34 (97%) tumors, whereas the ED SUV time–activity curves showed a nadir tumor signal beneath the liver level in approximately 40%–50% of tumors. This discrepancy, reported for static CE morphologic imaging methods (*6,21*), obviously reflects a visual underestimation of the degree of washout in images, probably due to the limited sensitivity of the human eye to differences in contrast and to the ED SUVmean–reducing effects of minor, nonvisible necrosis. The finding suggests that it may be necessary to calculate ED SUV time–activity curves to confirm visual classifications of washout, which generally is more gradual, and hence harder to see, than is tracer influx.

FIGURE 4. (Left) Time–activity curves of tumor ROI and liver ROI. (Right) ROIs themselves. Tumor curves show faster influx and higher peaks than liver tissue, followed by slower drop, which reached nontumor levels after more than 3 min, representing late washout. Red dotted line = ED SUVmax; red solid line = ED SUVmean; green dotted line = ED SUVmax; green solid line = ED SUVmean.
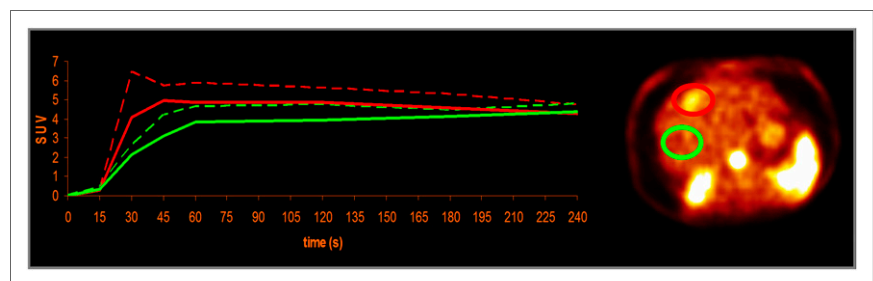
TABLE 3
Visual Evaluation of ED ^{18}F-FDG PET Time–Intensity Curves: Tumor Versus Nontumor Tissue

Visual curve evaluation	ED SUVmax	ED SUVmean
Arterial time window		
Earlier peak ED SUV in tumor vs. nontumor	34 (100)	34 (100)
Higher peak ED SUV in tumor vs. nontumor	29 (85)	18 (53)
Washout		
Nadir tumor signal below liver level	14 (41)	17 (50)
Nadir tumor signal at liver level	12 (35)	11 (32)
Nadir tumor signal above liver level	8 (24)	6 (18)

Data in parentheses are percentages.

Although less needed with focal accumulation, such confirmation would add confidence to visual classifications of that phenomenon.

Compared with other ED ^{18}F-FDG PET or CE CT studies (*19,21,22*), we found a relatively late peak signal in time–activity curves for both tumor and nontumor tissue. This observation is explained by the fact that we did not adjust our measurements by γ-variate fitting—that is, we did not use a mathematic function to exclude recirculation (*19,23*). We made this choice because, as previously noted, this pilot study sought to test ED ^{18}F-FDG PET as a CE CT–like procedure not to estimate blood flow as exactly as possible. Furthermore, with approximately 250 MBq of ^{18}F-FDG activities, a relatively low ED PET counting rate can be expected, and thus with MR imaging material measurement errors can occur in γ-variate fitting (*24*).

The ED ^{18}F-FDG PET methodology assessed here had certain limitations. First, we compared ED ^{18}F-FDG PET images side by side with separately obtained arterial CE CT images. Because ED ^{18}F-FDG PET took place with patients in the resting expiratory position, whereas CE CT was performed earlier during deeper inspiration, discrepant respiratory phase–induced liver displacements and deformations (*25*) and patient positioning complicated functional–anatomic correlation. Therefore, particularly when we quantitatively compared tumor versus liver ROIs, adjacent layers had to be closely scrutinized to differentiate actual focal findings from false-positive readings due to truncated vessels. The suboptimal coregistration also made it relatively time-consuming to find morphologic correlates for smaller foci and, together with the relatively low PET resolution (~4 mm) (*26,27*), would render it difficult to detect lesions less than

1 cm in diameter (*28*). For this last reason, similarly to Bernstine et al. (*19*), we included in our study only tumors of 1.5 cm or more. However, recently released software permitting ED ^{18}F-FDG PET and CE CT scan coregistration should ease functional–morphologic image correlation, enhancing identification of smaller nodules.

A second methodologic limitation of the studied ED ^{18}F-FDG PET was an inability to fit peripheral portions of greatly enlarged livers into the scanning area. This deficiency would of course be more marked in PET systems with smaller fields of view than our equipment had. Our scanner's fourth detector ring and the resultant comparatively large 21.8-cm axial field of view of 21.8 cm per bed position enabled complete liver registration in 22 of 27 patients (82%), whereas in the others, although the caudal portion of segment VI was not displayed, 90% or more of the liver was. Regardless of the field of view of the PET system, future software upgrades should allow large areas including several bed positions to be scanned with ED PET, permitting in at least some scanners complete registration, even in cases of extreme hepatomegaly.

In addition, many, but not all, PET scanners can perform the ED procedure. Hardware and, especially, software capable of list-mode acquisition and data evaluation are required.

Our study itself also had limitations. Because it was a pilot trial, no sample size calculation was performed. Additionally, the patient cohort was small, and no comparison was made with CE ultrasonography, CE MR imaging, or angiography. Further studies should be performed addressing these issues, and several additional avenues of investigation may be of interest. First, further protocol simplification may be possible. For example, our finding

TABLE 4
Quantitative ED ^{18}F-FDG PET Time–Activity Curve Evaluation

Variable	Tumor	Nontumor	*P*, Wilcoxon test
Time to peak ED SUVmax (s)	39 ± 15	90 ± 26	<0.05
Time to peak ED SUVmean (s)	73 ± 38	122 ± 43	<0.05
Peak ED SUVmax	10.7 ± 3.0	7.8 ± 1.9	<0.05
Peak ED SUVmean	6.7 ± 2.2	6.2 ± 1.7	0.39
Rate of ED SUVmax rise to peak (SUV/s)	0.30 ± 0.13	0.09 ± 0.04	<0.05
Rate of ED SUVmean rise to peak (SUV/s)	0.19 ± 0.09	0.07 ± 0.03	<0.05

that all HCCs but one reached a maximum early tracer accumulation by 60 s suggests that it may suffice to acquire only three 15-s frames in the arterial, portal venous, and venous time windows, analogous to CE CT imaging. The image stacks then could be evaluated with a simple Digital Imagining and Communications in Medicine viewer, obviating dedicated list-mode evaluation software and reducing computation time. Second, ED ^{18}F-FDG PET to assess HCC histologic differentiation should be explored, because CT arterioportography studies have established that this variable correlates with the extent of tumor vascularization (29). Lastly, ED ^{18}F-FDG PET could be evaluated in cirrhosis assessment, a purpose for which blood flow measurement by CE ultrasonography or CE MR imaging has been applied (30).

CONCLUSION

This pilot study provides initial proof of principle that a simplified ED ^{18}F-FDG PET/CT protocol with standard tracer activities, using visual examination of liver ED ^{18}F-FDG PET images and comparison of tumor versus liver ED SUV time–activity curves, effectively detects hypervascularization of HCC liver nodules of 1.5 cm or greater. These results suggest that this protocol can be easily added onto conventional static WB ^{18}F-FDG PET/CT in everyday practice. ED ^{18}F-FDG PET/CT using even further streamlined methodology might replace or supplement established CE morphologic imaging of HCC, especially in patients with contraindications to CT, ultrasonography, or MR imaging contrast medium or those procedures themselves.

DISCLOSURE

REFERENCES

1. Tajima T, Honda H, Taguchi K, et al. Sequential hemodynamic change in hepatocellular carcinoma and dysplastic nodules: CT angiography and pathologic correlation. *AJR.* 2002;178:885–897.
2. Namasivayam S, Salman K, Mittal PK, Martin D, Small WC. Hypervascular hepatic focal lesions: spectrum of imaging features. *Curr Probl Diagn Radiol.* 2007;36:107–123.
3. Shah RP, Brown KT, Sofocleous CT. Arterially directed therapies for hepatocellular carcinoma. *AJR.* 2011;197:W590–602.
4. Strobel D, Bernatik T. Diagnosis of focal liver lesions: importance of contrast enhanced ultrasound [in German]. *Dtsch Arztebl.* 2006;103:789–793.
5. Jung G, Cohnen M, Poll LW, Koch JA, Mödder U. Value of CT and MRI in the diagnosis of hepatic malignancies [in German]. *Onkologie.* 2003;9:263–271.
6. Jang HJ, Kim TK, Burns PN, Wilson SR. Enhancement patterns of hepatocellular carcinoma at contrast-enhanced US: comparison with histologic differentiation. *Radiology.* 2007;244:898–906.
7. Hollowell JG, Staehling NW, Flanders WD, et al. Serum TSH, T(4), and thyroid antibodies in the United States population (1988 to 1994): National Health and Nutrition Examination Survey (NHANES III). *J Clin Endocrinol Metab.* 2002;87:489–499.
8. Coresh J, Selvin E, Stevens LA, et al. Prevalence of chronic kidney disease in the United States. *JAMA.* 2007;298:2038–2047.
9. Namasivayam S, Kalra M, Torres W, Small W. Adverse reactions to intravenous iodinated contrast media: a primer for radiologists. *Emerg Radiol.* 2006;12:210–215.
10. Prokop M, Galanski M. *Whole-Body Tomography.* New York, NY: Thieme; 2007:100–101.
11. Brenner D, Elliston C, Hall E, Berdon W. Estimated risks of radiation-induced fatal cancer from pediatric CT. *AJR.* 2001;176:289–296.
12. Piscaglia F, Nolsoe C, Dietrich CF, et al. The EFSUMB Guidelines and Recommendations on the Clinical Practice of Contrast Enhanced Ultrasound (CEUS): update 2011 on non-hepatic applications. *Ultraschall Med.* 2012;33:33–59.
13. Hanna RF, Kased N, Kwan SW, et al. Double-contrast MR imaging for accurate staging of hepatocellular carcinoma in patients with cirrhosis. *AJR.* 2008;190: 47–57.
14. Khan MA, Combs CS, Brunt EM, et al. Positron emission tomography scanning in the evaluation of hepatocellular carcinoma. *J Hepatol.* 2000;32:792–797.
15. Shiomi S, Kawabe J. Clinical applications of positron emission tomography in hepatic tumors. *Hepatol Res.* 2011;41:611–617.
16. Mazzaferro V, Bhoori S, Sposito C, et al. Milan criteria in liver transplantation for hepatocellular carcinoma: an evidence-based analysis of 15 years of experience. *Liver Transpl.* 2011;17:S44–S57.
17. Ippolito D, Sironi S, Pozzi M, et al. Perfusion computed tomographic assessment of early hepatocellular carcinoma in cirrhotic liver disease: initial observations. *J Comput Assist Tomogr.* 2008;32:855–858.
18. Mullani NA, Herbst RS, O'Neil RG, Gould KL, Barron BJ, Abbruzzese JL. Tumor blood flow measured by PET dynamic imaging of first-pass ^{18}F-FDG uptake: a comparison with ^{15}O-labeled water-measured blood flow. *J Nucl Med.* 2008;49:517–523.
19. Bernstine H, Braun M, Yefremov N, et al. FDG PET/CT early dynamic blood flow and late standardized uptake value determination in hepatocellular carcinoma. *Radiology.* 2011;260:503–510.
20. Boellaard R, O'Doherty MJ, Weber WA, et al. FDG PET and PET/CT: EANM procedure guidelines for tumour PET imaging: version 1.0. *Eur J Nucl Med Mol Imaging.* 2010;37:181–200.
21. Valsecchi MG, Fazio F, Ippolito D, et al. Perfusion computed tomographic assessment of early hepatocellular carcinoma in cirrhotic liver disease: initial observations. *J Comput Assist Tomogr.* 2008;32:855–858.
22. Lin CY, Chen JH, Liang JA, Lin CC, Jeng LB, Kao CH. ^{18}F-FDG PET or PET/CT for detecting extrahepatic metastases or recurrent hepatocellular carcinoma: a systematic review and meta-analysis. *Eur J Radiol.* 2012;81:2417–2422.
23. Davenport R. The derivation of the gamma-variate relationship for tracer dilution Curves. *J Nucl Med.* 1983;24:945–948.
24. Benner T, Heiland S, Erb G, Forsting M, Sartor K. Accuracy of gamma-variate fits to concentration-time curves from dynamic susceptibility-contrast enhanced MR imaging: influence of time resolution, maximal signal drop and signal-to-noise. *Magn Reson Imaging.* 1997;15:307–317.
25. Clifford MA, Banovac F, Levy E, Cleary K. Assessment of hepatic motion secondary to respiration for computer assisted interventions. *Comput Aided Surg.* 2002;7:291–299.
26. Jakoby BW, Bercier Y, Watson CC, et al. Physical Performance and Clinical Workflow of a new LSO HI-REZ PET/CT Scanner. *IEEE Nucl Sci Symp Conf Rec.* 2006;5:3130–3134.
27. Saha G. *Basics of PET Imaging: Physics, Chemistry, and Regulations.* New York, NY: Springer; 2010:97–100.
28. Soret M, Bacharach SL, Buvat IN. Partial-volume effect in PET tumor imaging. *J Nucl Med.* 2007;48:932–945.
29. Asayama Y, Yoshimitsu K, Nishihara Y, et al. Arterial blood supply of hepatocellular carcinoma and histologic grading: radiologic-pathologic correlation. *AJR.* 2008;190:W28–W34.
30. Annet L, Materne R, Danse E, Jamart J, Horsmans Y, Van Beers BE. Hepatic flow parameters measured with MR imaging and Doppler US: correlations with degree of cirrhosis and portal hypertension. *Radiology.* 2003;229:409–414.